Plasmonics
DOI 10.1007/s11468-016-0449-1

Nanoscale Dielectric Function of Fe, Pt, Ti, Ta, Al, and V: Application to Characterization of Al Nanoparticles Synthesized by Fs Laser Ablation

Luis J. Mendoza Herrera [1] · David Muñetón Arboleda [1] · Jesica M. J. Santillán [1,2] · Marcela B. Fernández van Raap [3,4] · Lucía B. Scaffardi [1,5] · Daniel C. Schinca [1,5]

Received: 23 May 2016 / Accepted: 25 November 2016

Abstract Development and applications of new nanomaterials and nanocomposites that include metal nanoparticles have received much attention in the last years. However, there are relatively few studies concerning basic physical characteristics of the dielectric function at the nanoscale, which is needed for predicting their optical and plasmonic response. The size-dependent complex dielectric function of metal Fe, Pt, Ti, Ta, Al, and V nanoparticles (NPs) is calculated for the first time for an extended wavelength range from UV to FIR, based on experimental bulk complex refractive index measurements in the mentioned range at room temperature. Calculation is based on a "top-down" approach, based on a stepwise modification of the Drude model. Bulk plasma frequency (ω_p) and damping constant (γ_{free}) in this model are determined using a method that improves the relative uncertainties in their values and provide an insight about the wavelength range over which the metal may be considered Drude like. Validation of ω_p and γ_{free} values is demonstrated by the improved accuracy with which the experimental bulk dielectric function is reproduced. For nanometric and subnanometric scales, dielectric function is made size dependent considering size-corrective terms for free and bound electron contributions to the bulk dielectric function. These results are applied to analyze the synthesis of Al NP suspensions using a 120-fs pulse laser to ablate an Al solid target in *n*-heptane and water. The presence of Al, Al-Al_2O_3, and air-Al core-shell structures is also reported for the first time in these type of colloids. Analysis of the structure, configuration, sizing, and relative abundance was carried out using optical extinction spectroscopy (OES). Sizing results are compared with those provided by atomic force microscopy (AFM) studies.

Keywords Metal nanoparticles · Dielectric function · Plasmon resonance

✉ Daniel C. Schinca
daniels@ciop.unlp.edu.ar

[1] Centro de Investigaciones Ópticas (CIOp) (CONICET La Plata-CIC-UNLP), CC3(1897) Gonnet, La Plata, Argentina

[2] Departamento de Química, Facultad de Ciencias Exactas y Naturales, UNCa, Av. Belgrano 300, 4700 San Fernando del Valle de Catamarca, Catamarca, Argentina

[3] Instituto de Física La Plata (IFLP), CONICET, Calle 49 y 115, 1900 La Plata, Buenos Aires, Argentina

[4] Departamento de Física, Facultad de Ciencias Exactas, UNLP, Calle 49 y 115, 1900 La Plata, Buenos Aires, Argentina

[5] Departamento de Ciencias Básicas, Facultad de Ingeniería, UNLP, Calle 1 y 47, 1900 La Plata, Argentina

Introduction

Optical properties of metal nanoparticles (NPs) are currently an active research field due to the basic plasmonic properties of nanoscale materials and their broad applications in several areas of science and technology. Until now, the vast majority of research has been devoted to noble metal NPs (Au, Ag, and Cu). With the advancement of new synthesis methods, other metal NPs are now being the center of intense research, since they can be used as part of composite materials. In particular, Fe, Pt, Ti, Ta, Al, and V NPs have important applications in therapeutics [1, 2], sensors [3–5], biology [6, 7], environment [8], materials sciences [9–11], catalysis [12, 13], plasmonic nanoantennas [14, 15], solar cells [16] and lithium battery cathodes [17], among others. Many of these applications

Published online: 08 December 2016

in the vis-NIR rely on the optical and plasmonic properties of these elements, which, in turn, depend on the complex dielectric function.

Metal dielectric function can be regarded as the sum of free (intraband transitions in the Drude model) and bound (interband transitions) electron contributions. These two terms must be modified when the size of NPs decreases down to a few nanometers, to account for electron confinement size effects. It is important then to determine the Drude metal bulk dielectric function parameters (plasma frequency (ω_p) and damping constant (γ_{free})) as a first step to calculate the size-dependent dielectric function of the studied NPs. Knowledge of this size-corrected dielectric function may prove very useful when using effective medium models to determine optical properties of composite materials that have these NPs embedded in a host, especially in the NIR-FIR, including the THz region. Besides, it may be used in effective medium models (Maxwell-

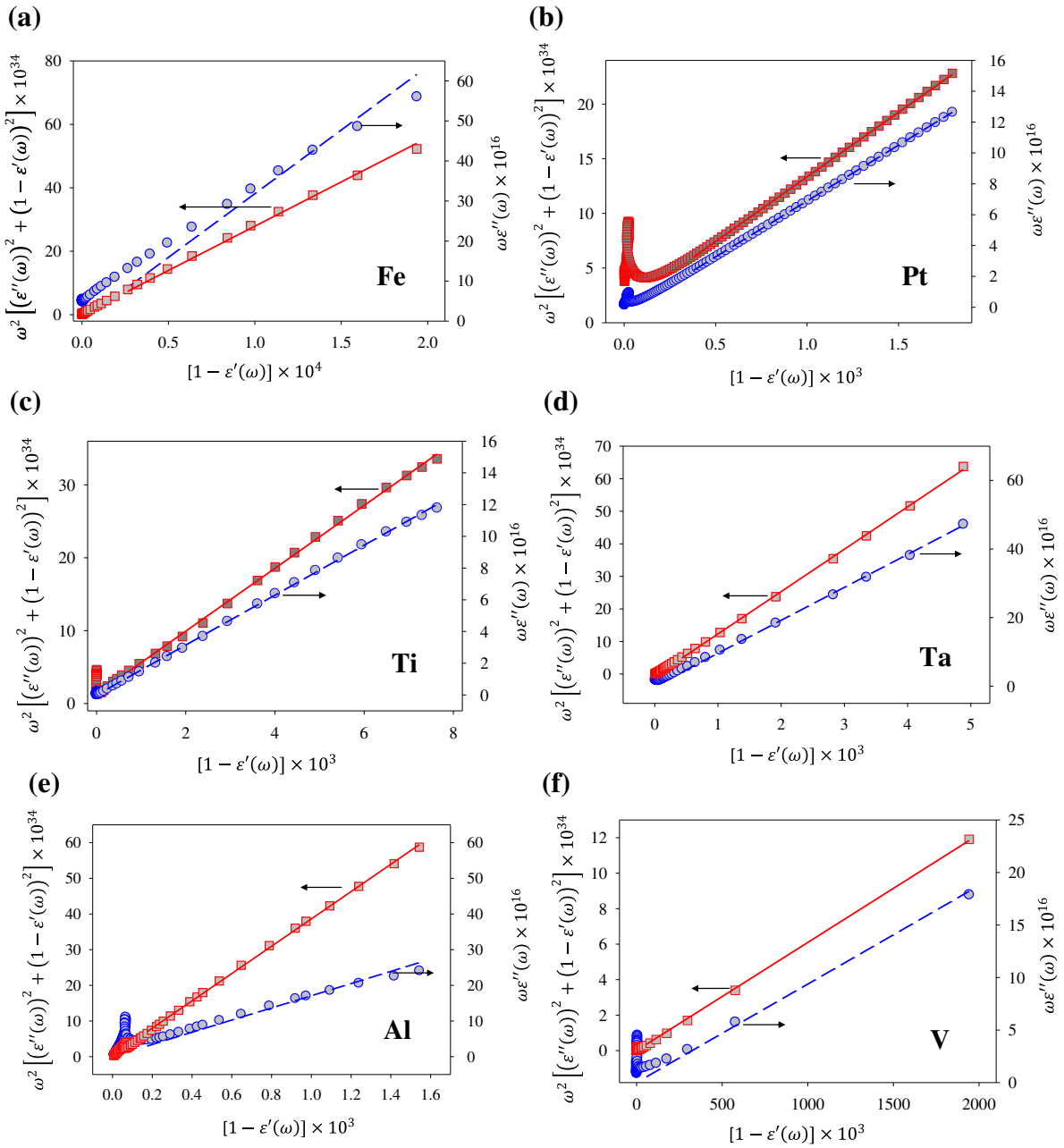

Fig. 1 Plots of Eqs. (2) and (3) are indicated by *circles* and *squares*, respectively. Linear regressions fit the experimental data for the wavelength range where the dielectric function can be described purely by the Drude model. The slopes of the linear regressions yield the values of γ_{free} (*dashed line*) and ω_p^2 (*full line*) for **a** Fe, **b** Pt, **c** Ti, **d** Ta, **e** Al, and **f** V. *Arrows* indicate the vertical axis corresponding to each function

Garnett, Brugerman, or others) to determine optical properties of global composite materials that have metal NPs embedded in a dielectric host.

In this work, we determine ω_p and γ_{free} for Fe, Pt, Ti, Ta, Al, and V using the experimental bulk dielectric function at large wavelengths, where the influence of bound electron transitions is negligible. The determination of these parameters is carried out using a procedure that lifts the commonly used restriction $\omega >> \gamma_{free}$ in the Drude expression, providing a wider wavelength applicability [18]. Then, we rewrite the full size-corrected dielectric function as the sum of three terms, one corresponding to the experimentally measured bulk values from UV-visible to NIR-FIR and two size-corrective contributions for free and bound electrons [19]. When the full size-dependent dielectric function is written in this way, the uncertainty in the calculated values corresponds to that of bulk experimental data. The correct determination of ω_p and γ_{free} is validated by the improved fitting of the bulk experimental dielectric function when their values are introduced in the expression of the size-dependent dielectric function.

Finally, the previous theoretical calculations are applied to analyze the extinction spectra of Al colloids generated by femtosecond laser ablation in *n*-heptane and water. From the fit of the spectra, species composition and sizing are obtained by optical extinction spectroscopy (OES). Size derived from AFM images is in good agreement with OES results.

Determination of ω_p and γ_{free}: Bulk Dielectric Function

The simplest approach to metal dielectric function is based on the so-called Drude model, which considers that electrons in the metal are essentially free and can be forced to oscillate when an electromagnetic wave of frequency ω is incident upon it. In this case, it can be readily shown that the metal dielectric function $\varepsilon_{free}(\omega)$ takes its simple form [20–22]:

$$\varepsilon_{free}(\omega) = 1 - \frac{{\omega_p}^2}{\omega^2 + i\omega\gamma_{free}} \quad (1)$$

where ω_p and γ_{free} were mentioned before.

If the real (ε') and imaginary (ε'') parts of Eq. (1) are written separately, it is possible to obtain two different linear relationships between them [18]:

$$\omega\varepsilon''(\omega) = \gamma_{free}\left(1-\varepsilon'(\omega)\right), \quad (2)$$

$$\omega^2\left[\left(\varepsilon''(\omega)\right)^2 + \left(1-\varepsilon'(\omega)\right)^2\right] = \omega_p^2\left(1-\varepsilon'(\omega)\right), \quad (3)$$

If the functions $\omega\ \varepsilon''(\omega)$ and $\omega^2[(\varepsilon''(\omega))^2 + (1-\varepsilon'(\omega))^2]$ are plotted against $(1-\varepsilon'(\omega))$, γ_{free} and ω_p^2 can be easily derived from the slopes of the curves defined by Eqs. (2) and (3).

Experimental values of the complex refractive index $(n + ik)$ for the studied metals are reported by different authors [23–27] for discrete wavelength values. These are specific for each metal, spreading from UV-visible to FIR as follows: from 0.667 to 286 μm for iron, from 0.206 to 12.4 μm for platinum, from 0.667 to 200 μm for titanium, from 0.667 to 14.3 μm for tantalum, from 0.0165 to 4 μm for aluminum, and from 0.031 to 12.407 μm for vanadium. The real and imaginary parts of the experimental dielectric function may be derived from the relations $\varepsilon'(\omega) = n(\omega)^2 - k(\omega)^2$ and $\varepsilon''(\omega) = 2\ n(\omega)\ k(\omega)$. Introducing the experimental $\varepsilon'(\omega)$ and $\varepsilon''(\omega)$ values for each metal into Eqs. (2) and (3) for the different frequencies given in [23–27], it is possible to plot the left sides of these equations as a function of $(1-\varepsilon'(\omega))$, as shown in Fig. 1. The data can be fitted by a linear regression in the frequency range where each metal satisfies the Drude model. Circles correspond to data for Eq. (2) and squares to data for Eq. (3). Arrows indicate the vertical axis corresponding to each function. From the slopes of the linear plots, γ_{free} and ω_p^2 can be determined.

Since the wavelength ranges over which the real and imaginary parts of the dielectric function differ for each metal, the abscissa axes have different scales. Data points in Fig. 1 can be linearly fitted with the zero ordinate

Table 1 Values of ω_p and γ_{free} determined in this work compared with values given by other authors

Metal	$\omega_p\ \left[\frac{rad}{s}\right] \times 10^{15}$	γ_{free} [rad/s] $\times 10^{13}$
Fe	5.167±0.024 (this work) 5.557 [23]	3.053±0.040 (this work) 2.939 [23]
Pt	8.327±0.030 (this work) 8.4078 [24]	13.136±0.632 (this work) 12.154 [24]
Ti	3.966±0.010 (this work) 4.710 [23] 4.2610 [24]	4.565±0.076 (this work) 7.008 [23] 12.458 [24]
Ta	11.406±0.080 (this work) 9.420 [23]	9.600±0.200 (this work) 8.855 [23]
Al	19.656±0.059 (this work) 17.465 [23] 16.459 [24]	17.073±0.690 (this work) 7.6867 [23] 7.141 [24]
V	7.8073 ± 0.039 (this work) 33.91 [26]	9.3775 ± 0.047 (this work) 8.7719 [26]

intercept according to Eqs. (2) and (3) only for the wavelength range in which the Drude model is satisfied. Data points in the extreme left of the plots depart strongly from a straight line, indicating that interband transitions dominate at smaller wavelengths.

Table 1 summarizes the values of ω_p and γ_{free} determined in this work at room temperature, together with those calculated by other authors, for comparison purposes. It can be seen that the method derived from Eqs. (2) and (3) is capable of determining both ω_p and γ_{free} simultaneously with small uncertainties. No mention of uncertainties is made by other authors.

With the obtained values of ω_p and γ_{free}, the real and imaginary parts of Eq. (1) can be fitted in the wavelength range for which the complex refractive index of each metal was experimentally determined [23–27]. Figure 2a–f plots $\varepsilon'(\omega)$ and $\varepsilon''(\omega)$ as a function of wavelength for Fe, Pt, Ti, Ta, Al, and V, respectively. Experimental bulk dielectric function data are represented by squares and circles for $\varepsilon'(\omega)$ and $\varepsilon''(\omega)$, respectively. Arrows indicate the

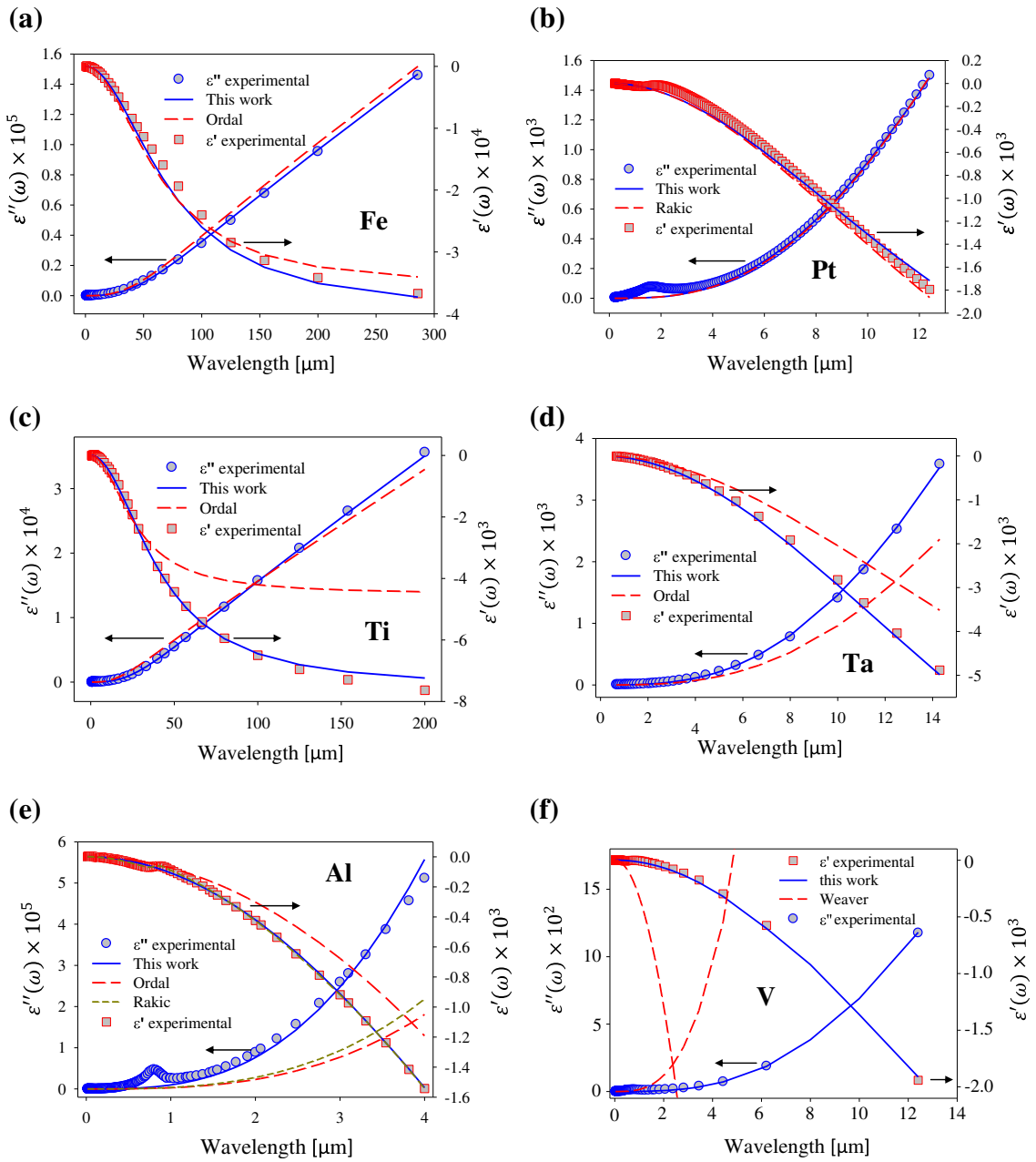

Fig. 2 Experimental real (*squares*) and imaginary (*circles*) parts of bulk dielectric function, respectively. *Full lines* represent the fit of the experimental data based on free electron contribution given by Eq. (1) using ω_p and γ_{free} values calculated in this work. *Dashed lines* represent the same calculation using ω_p and γ_{free} values given by other authors listed in Table 1. Panels correspond to **a** Fe, **b** Pt, **c** Ti, **d** Ta, **e** Al, and **f** V

vertical axis corresponding to each function. Full lines represent the fit using ω_p and γ_{free} values determined in this work, while dashed lines show the fit using the parameter values given by the authors cited in Table 1 (named in the panels of Fig. 2).

It can be seen that our method for the determination of ω_p and γ_{free} allows reproducing with high reliability the behavior of the bulk dielectric function in a wide wavelength range from UV-visible-NIR to FIR. For certain elements, such as Ti, Ta, Al, and V, theoretical calculations using the parameters reported by other authors mentioned in Table 1 depart strongly from the experimental bulk values for NIR-FIR wavelengths. Instead, our method allows a much better fit of the measured dielectric function in this range, as well as to the visible-UV.

Size-Dependent Dielectric Function at the Nanoscale

Having obtained a reliable bulk dielectric function, we are ready to build the appropriate size-dependent expression for nanosized spheres. Metal dielectric function may be considered as an additive contribution of free and bound electron terms. As mentioned in the previous section, free electrons can be described with the well-known Drude model (Eq. 1), while the bound electron term contains contributions from interband transitions which, in general, depend on the band shapes of the particular studied metal. With these assumptions, the bulk dielectric function can be written as [28, 29]

$$\varepsilon_{bulk}(\omega) = \varepsilon_{free}(\omega) + \varepsilon_{bound}(\omega), \tag{4}$$

where $\varepsilon_{bulk}(\omega)$ is the experimentally determined dielectric function.

For spherical NPs under about 10 nm radius (depending on the specific metal), electron collisions with the particle boundary begin to have a relevant role in electron dynamics. A size-dependent expression for the free electron damping constant of the form $\gamma_{size} = \gamma_{free} + C\frac{v_F}{R}$ [22, 30] is often introduced to account for the reduced mean free path, v_F being the Fermi velocity and C a constant that depends on the material, having a value of about 0.8. The free electron contribution can now be written as

$$\varepsilon_{free}(\omega, R) = 1 - \frac{{\omega_p}^2}{\omega^2 + i\omega\gamma_{free} + i\omega C\frac{v_F}{R}} \tag{5}$$

For NPs about an order of magnitude smaller, bound electron contribution must also be size modified to take into account the decrease in energy level density within bands, through an expression that takes the form $\varepsilon_{bound}(\omega, R) = \varepsilon_{bound}(\omega)(1 - \exp(-R/R_0))$ [31–33] where R_0 is a reference radius value. With the above corrections, the full size-dependent dielectric function of spherical NPs can be written as a function of frequency and radius as

$$\varepsilon(\omega, R) = \varepsilon_{free}(\omega, R) + \varepsilon_{bound}(\omega, R) \tag{6}$$

Making a suitable regrouping of terms, the general size-dependent dielectric function can be expressed as the sum of three terms: the experimental bulk dielectric function, a size-corrective term for free electron contribution (which includes ω_p and γ_{free}), and a size-corrective term for bound electron contribution

$$\varepsilon(\omega, R) = \varepsilon_{bulk}(\omega) + \Delta\varepsilon_{free}(\omega, R) + \Delta\varepsilon_{bound}(\omega, R) \tag{7}$$

where

$$\Delta\varepsilon_{free}(\omega, R) = \frac{{\omega_p}^2}{\omega}\left(\frac{iCv_F/R}{(\omega + i\gamma_{free})\left(\omega + i\gamma_{free} + iCv_F/R\right)}\right) \tag{8}$$

and

$$\Delta\varepsilon_{bound}(\omega, R) = \exp\left(-R/R_0\right)\left(\varepsilon_{bulk}(\omega) - 1 + \frac{{\omega_p}^2}{(\omega^2 + i\omega\gamma_{free})}\right) \tag{9}$$

In this way, the expressions for $\Delta\varepsilon_{free}(\omega, R)$ and $\Delta\varepsilon_{bound}(\omega, R)$ in Eqs. (8) and (9) may be regarded as size-dependent corrective terms to the experimental dielectric function $\varepsilon_{bulk}(\omega)$ (Eq. 4). Based on Eqs. (7), (8), and (9), $\varepsilon'(\omega, R)$ and $\varepsilon''(\omega, R)$ were calculated for the studied metals for several NP radii and shown in Figs. 3, 4, 5, 6, 7, and 8. Since the dielectric functions were reported in [23, 24] and [26] for wavelengths larger than 700 nm, data given in [27] were used for calculations at smaller wavelengths. Values of ω_p and γ_{free} for each metal were taken from our results shown in Table 1, while values of Fermi velocity were taken from the literature and are shown in Table 2.

In all figures, squares and circles correspond to experimental data. It can be observed that for decreasing sizes between 50 and 20 nm (depending on the metal), the dielectric function still behaves very much like bulk.

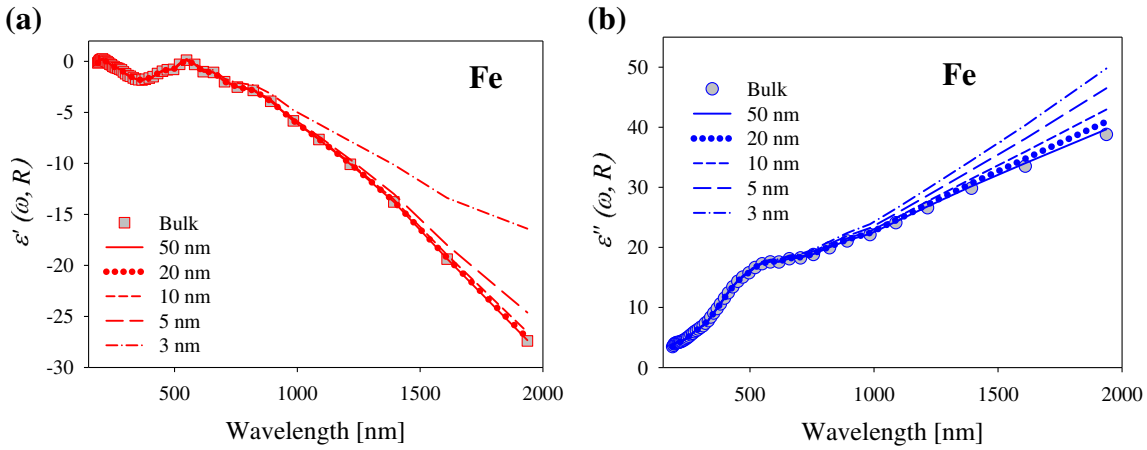

Fig. 3 Theoretical values for real (**a**) and imaginary (**b**) parts of iron dielectric function as a function of wavelength for different radii. Experimentally derived bulk values are represented by *squares* and *circles*

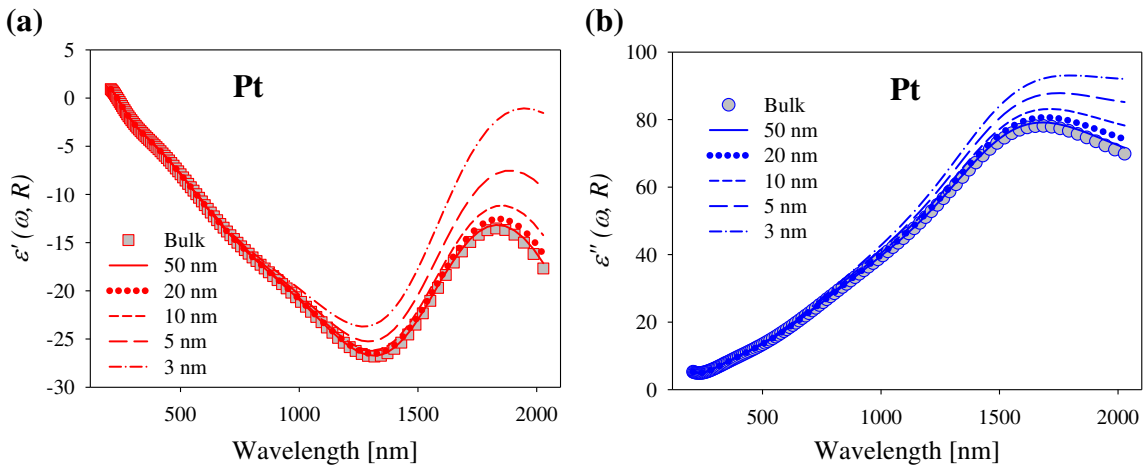

Fig. 4 Theoretical values for real (**a**) and imaginary (**b**) parts of platinum dielectric function as a function of wavelength for different radii. Experimentally derived bulk values are represented by *squares* and *circles*

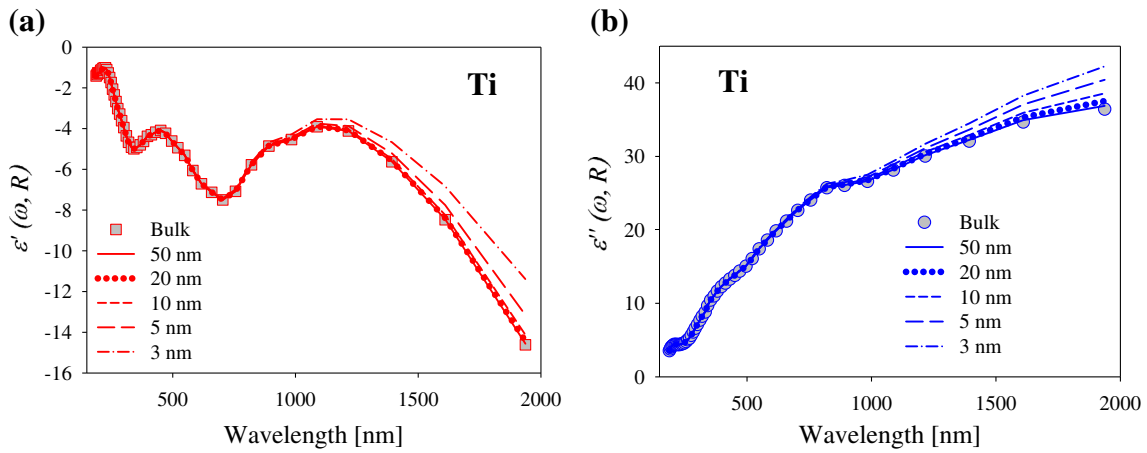

Fig. 5 Theoretical values for real (**a**) and imaginary (**b**) parts of titanium dielectric function as a function of wavelength for different radii. Experimentally derived bulk values are represented by *squares* and *circles*

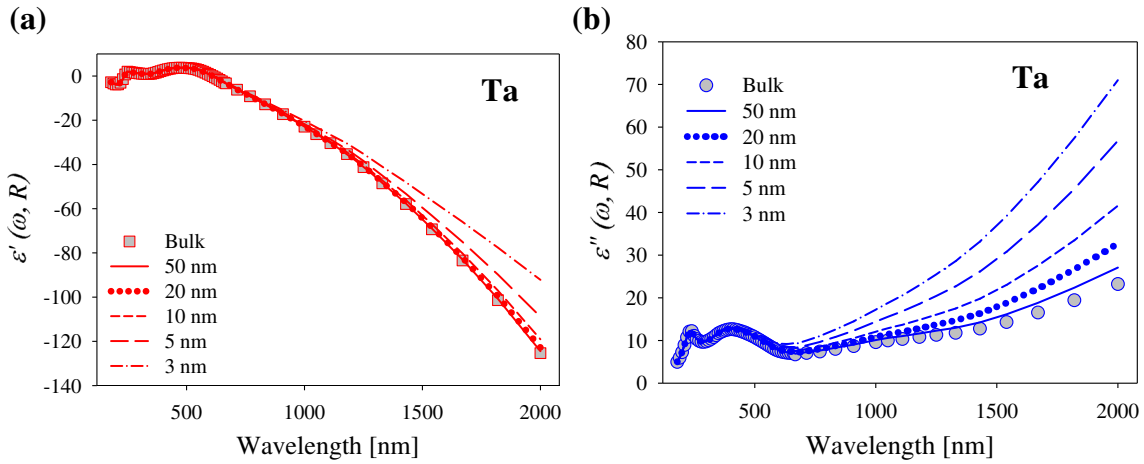

Fig. 6 Theoretical values for real (**a**) and imaginary (**b**) parts of tantalum dielectric function as a function of wavelength for different radii. Experimentally derived bulk values are represented by *squares* and *circles*

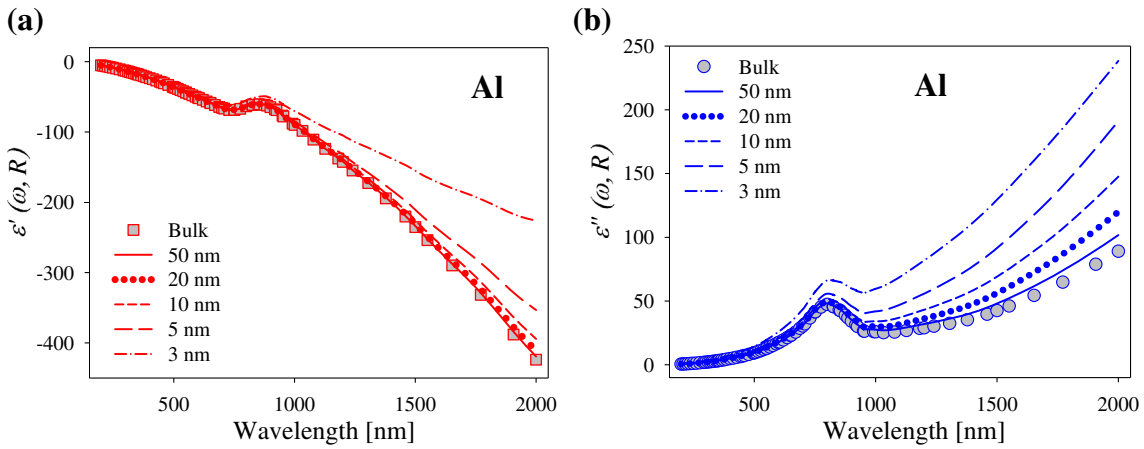

Fig. 7 Theoretical values for real (**a**) and imaginary (**b**) parts of aluminum dielectric function as a function of wavelength for different radii. Experimentally derived bulk values are represented by *squares* and *circles*

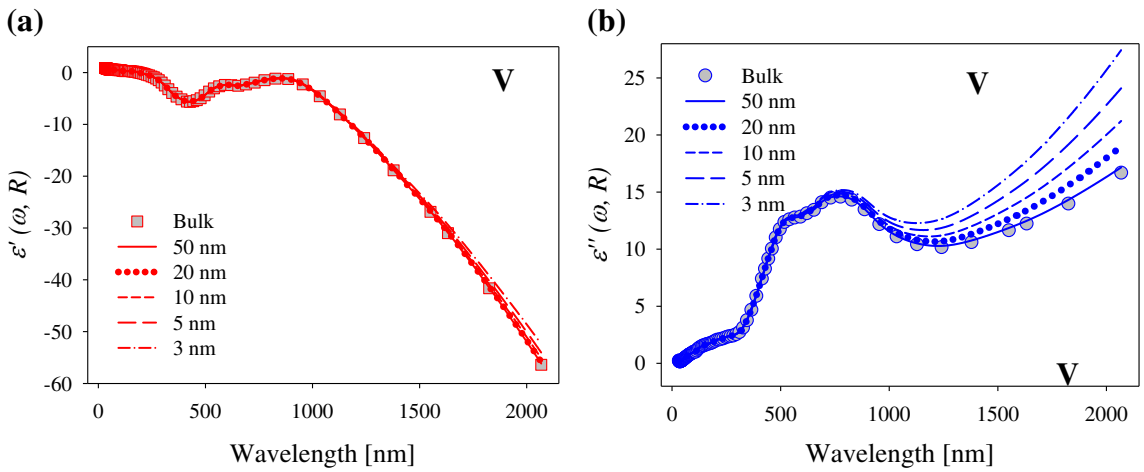

Fig. 8 Theoretical values for real (**a**) and imaginary (**b**) parts of vanadium dielectric function as a function of wavelength for different radii. Experimentally derived bulk values are represented by *squares* and *circles*

Table 2 Values of Fermi velocity used for calculations of $\varepsilon'(\omega, R)$ and $\varepsilon''(\omega, R)$

Metal	$v_F \times 10^{15}$ [nm/s]	References
Fe	1.72	[34]
Ti	1.73	[35]
Ta	1.72	[36]
Pt	1.45	[37]
Al	2.03	[34]
V	0.372	[38]

Table 3 NP species present in Al colloids fabricated by laser ablation in *n*-heptane

Species	External radius R_m [nm]	σ	Shell (% R_1)	Total relative abundance [%]
Al	14.4	0.54	0	89
Air-Al	29.8	0.15	11	9
Air-Al	30.6	0.52	21	2

However, for NP radii smaller than 10 nm (depending on the metal), there is a general departure from the bulk behavior, especially for wavelengths larger than 750 nm. This departure is due to the influence of the size-corrective terms for free and bound electron contributions, as indicated in Eq. (7).

The strength of our method is that it allows calculating the size-dependent dielectric function for any size and, for 50 nm (size for which all metals behave like bulk), theoretical curves accurately fit the experimental values reported in the literature.

In previous works devoted to the study of noble metal nanoparticles [31–33, 39] we concluded that, while both corrections on the complex dielectric function are present for sizes smaller than 50 nm, $\Delta\varepsilon_{bound}(\omega, R)$ is negligible for sizes down to about 2 or 3 nm, depending on the metal. For smaller radii (down to about 0.7 nm), the latter correction must be taken into account to describe the metal dielectric function. Similar calculations carried out for the metals studied in this work also show that the influence of the bound electron corrective term is noticeable for sizes smaller than 2 nm.

Application to Sizing Al NPs Fabricated by Femtosecond Laser Ablation

When the size-dependent metal dielectric function is used as an input to Mie theory, structure, configuration, and size distribution of spherical metal NPs can be derived. To show the ability of OES to characterize metal colloids, we apply it in this paragraph to one of the studied metals. Aluminum nanostructures have become a very active area of research since, in contrast to noble metals, aluminum exhibits good plasmonic properties in the UV, it is compatible with complementary metal-oxide-semiconductor (CMOS) technology [40], and it is low cost and widely available. Its plasmonic properties are useful in photocatalysis [41], fluorescence enhancement [42] and nanofocusing of ultraviolet light [43], among others. Due to these possible applications, we selected aluminum to apply our previous results for NP sizing.

Aluminum colloids were fabricated using pulsed laser ablation in liquids (PLAL). A 1-mm-thick solid disk of high-purity-grade aluminum was immersed in a vessel filled with 4 cm^3 of *n*-heptane or Milli-Q water. Laser ablation of the Al disk was performed using a Ti:sapphire (Ti:Sa) chirped pulsed

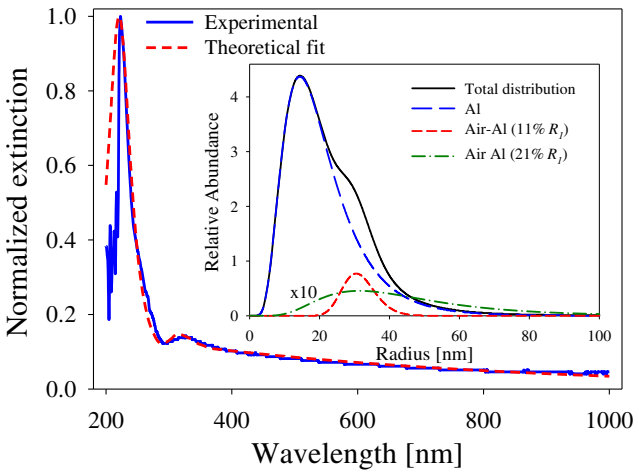

Fig. 9 Experimental extinction spectrum of Al NPs fabricated by laser ablation in *n*-heptane (*full line*). Theoretical fit (*dashed line*) using Mie theory with the size-dependent metal dielectric function determined in this work. The *inset* shows the relative abundance and size distribution of the species derived from the optimum fit. The *dashed-dotted line* is multiplied by a factor of 10 to make it visible in the same scale

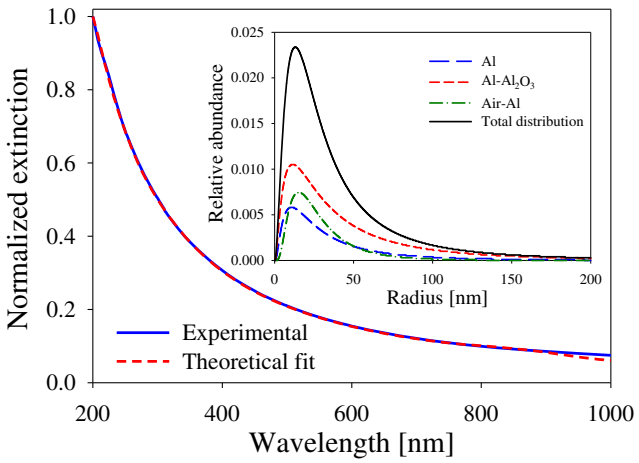

Fig. 10 Experimental extinction spectrum of Al NPs fabricated by laser ablation in water (*full line*) with 500 μJ pulse energy. Theoretical fit (*dashed line*) using Mie theory with the size-dependent metal dielectric function determined in this work. The *inset* shows the species size distribution derived from the optimum fit

Table 4 NP species present in Al colloids produced by laser ablation in water

Species	External radius R_m [nm]	σ	Shell (% R_1)	Total relative abundance [%]
Al	10.8	0.94	0	23
Al-Al_2O_3	11.3	1.03	19.4	53
Air-Al	15.1	0.67	20.3	24

amplification (CPA) system from Spectra Physics, emitting pulses of 120 fs with a 1-kHz repetition rate centered at 800-nm wavelength. The maximum output energy was 1 mJ per pulse, but it could be attenuated using a classical waveplate-polarizer system. The laser beam was focused on the target disk surface by a 5-cm focal length lens. The sample was moved using an *XY* motorized micrometric stage.

AFM images of aluminum colloid samples were recorded in air, at room temperature, and at a scan rate of 1 Hz, using the standard semicontact mode of an NT-MDT Solver Pro microscope. Rectangular-shaped cantilevers coated with aluminum on the reflex side, with a spring constant of 37–58 N/m and holding a pyramidal silicon tip of 6-nm curvature radius, were used for topographical measurements. The AppNano ACTA probe at resonant frequencies of 300 kHz was used to scan NPs prepared in water. For these measurements, part of the as-prepared colloidal suspension was sonicated and diluted to 1/100 (*v*/*v*) in water, placed on a freshly cleaved muscovite mica sheet V-1 grade (SPI Supplies), and dried for 10 min at 40 °C temperature.

Figure 9 shows the extinction spectra of Al NPs fabricated in *n*-heptane using 500 μJ laser pulse energy. Notice that there is a clear plasmon peak at 223 nm and a smaller absorption peak at 327 nm. The spectrum is fitted based on bare Al (radius R_1) and air-Al (external radius R_2) NP species, the latter with two different Al thicknesses. No oxidized species appear since oxidation in the ablation plume may be assumed almost non-existent due to the absence of oxygen in *n*-heptane. Log-normal size distribution and composition that resulted from the theoretical fit are added as an inset, which shows the relative abundance of the two NP species present in the colloid: Al bare-core and hollow-Al (air-Al). The former accounts for the majority of the NPs, while the latter appears in the least amount and with two different shell thicknesses (11% R_1 and 21% R_1). The size distribution of air-Al NPs with the larger shell thickness (dashed-dotted line) is multiplied by a factor of 10 to make it visible in the same scale as the others.

Table 3 summarizes the species, modal external radius R_m, scale parameter σ, shell thickness, and total relative abundance [%] corresponding to the inset of Fig. 9.

Figure 10 shows the extinction spectrum of Al NPs in water also for 500 μJ laser pulse energy. In contrast to the case of *n*-heptane, no plasmon peak is observed. Both the growth of an oxide shell around Al NPs due to the presence of oxygen (molecular and atomic) in the ablation plume and a broader size distribution are the causes of the disappearance of the plasmon resonance. The experimental spectrum is fitted based on bare-Al, Al-Al_2O_3, and air-Al NP species. The inset in Fig. 10 shows that the species size distribution is quite broad, reaching sizes of about five to six times the modal radius.

Table 4 summarizes the main results derived from fitting spectrum. The external radius R_m corresponds to the modal radius of the partial size distribution of each species indicated in the inset of Fig. 10. The most abundant is oxidized as Al-Al_2O_3, while Al bare-core and air-Al NPs appear in almost equal proportion.

Independent AFM analysis carried out over the same sample supports sizing results derived from OES. Figure 11a shows a panoramic 40 μm × 20 μm area image where several isolated NPs are observed. Panel b shows the height profile (diameter) of some sampled particles indicated by the dashed lines drawn in panel a. It can be seen that the radius values are in the range 40 to 110 nm.

To sample medium and smaller particles, the scanned image area was reduced. Figure 12a shows a 14 μm × 14 μm

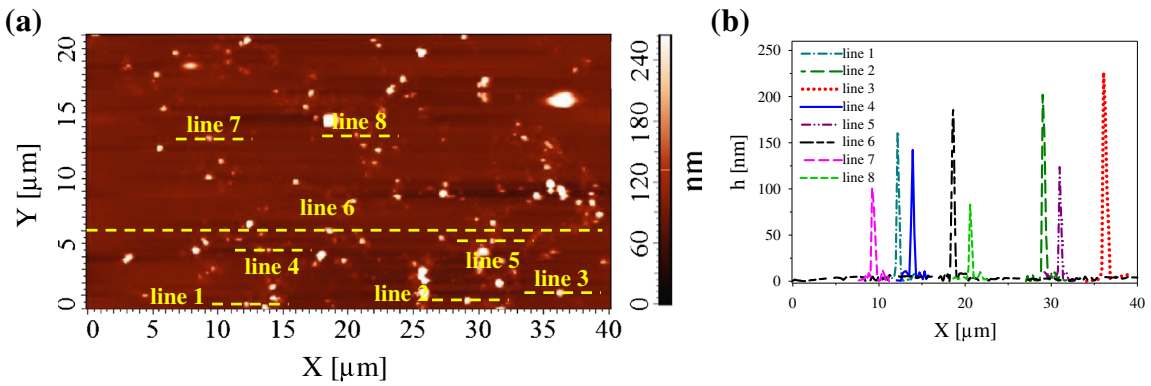

Fig. 11 **a** AFM 40 μm × 20 μm area image of Al NPs generated by laser ablation with 500 μJ pulse energy. The profile (height) of sampled NPs indicated by the *dashed lines* drawn across them is shown in **b**

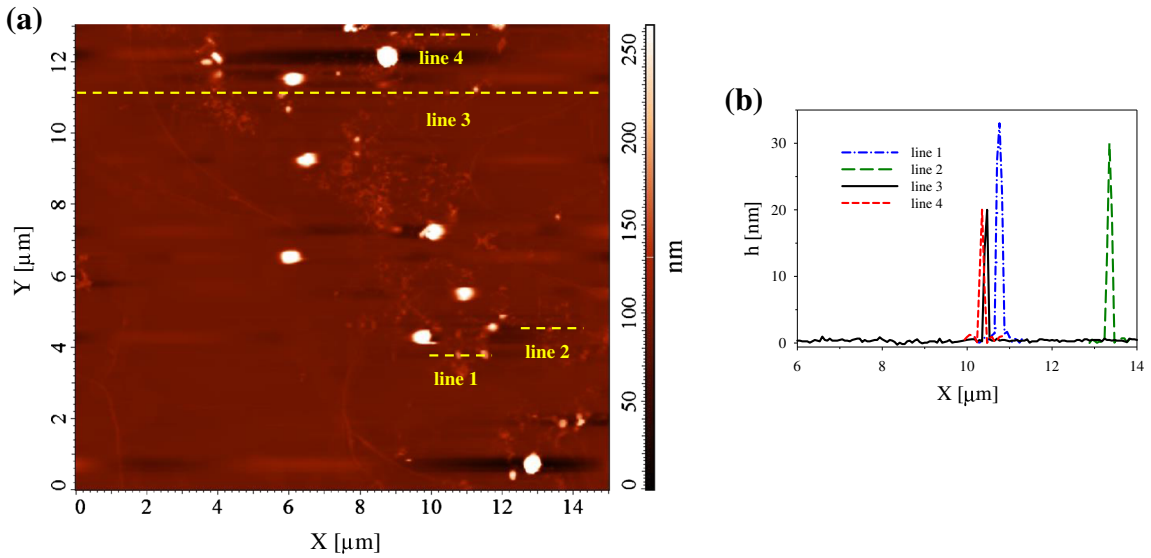

Fig. 12 **a** AFM 14 μm × 14 μm area image of Al NPs generated by laser ablation with 500 μJ pulse energy. The *dashed lines* drawn across certain NPs show their profile (height) in **b**

area, for which the sampled NPs have radius values in the range 20 to 40 nm, as can be seen in panel b.

Figure 13a shows an even smaller area of 2 μm × 2 μm, for which the sampled NPs have radius values in the range 4 to 15 nm, as can be seen in panel b

Conclusions

We have simultaneously determined the parameters ω_p and γ_{free} for Fe, Pt, Ti, Ta, Al, and V metals from the slope of linear fits of relations between $\varepsilon'(\omega)$ and $\varepsilon''(\omega)$ for large wavelengths, avoiding the traditional approximation $\omega >> \gamma_{free}$ which restricts frequency values to the UV-deep UV region. The values of ω_p and γ_{free} obtained using our method allow fitting the experimental discrete values of the bulk dielectric function of the mentioned metals with larger accuracy in the UV-visible and especially extending to NIR-FIR. The continuous function so obtained allows calculating the bulk dielectric function for any wavelength.

The obtained parameters were then introduced in the expression for the full size-dependent dielectric function to

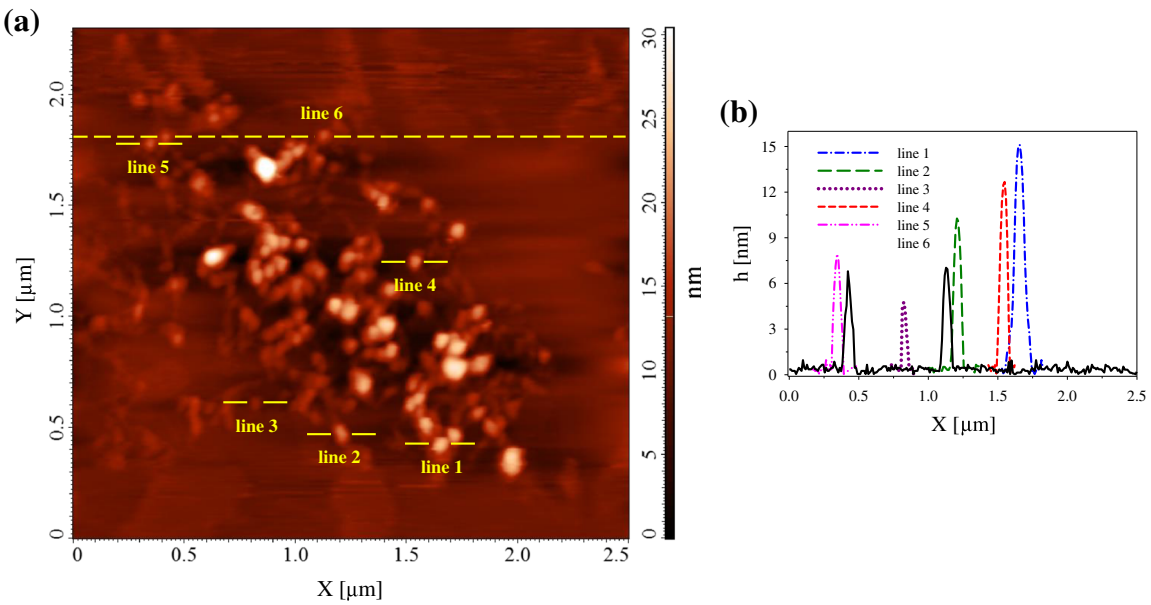

Fig. 13 **a** AFM 2 μm × 2 μm area image of Al NPs generated by laser ablation with 500 μJ pulse energy. The *dashed lines* drawn across certain NPs show their profile (height) in **b**

analyze its behavior with size. The expression is rewritten as the sum of three terms: the experimental bulk dielectric function, a size-corrective term for free electron ($\Delta\varepsilon_{free}(\omega, R)$), and a size-corrective term for bound electron contribution ($\Delta\varepsilon_{bound}(\omega, R)$). The main advantage of this approach is that the uncertainty in the dielectric function determination is mainly due to that of the bulk experimental data. The influence of the term $\Delta\varepsilon_{free}(\omega, R)$ is important for radii below 10 nm, while the influence of $\Delta\varepsilon_{bound}(\omega, R)$ is noticeable for radii below 5 nm. The expression of the size-corrected dielectric function allows predicting very accurately the optical properties of small metal NPs in the NIR-FIR range.

The introduction of the determined size-dependent dielectric function in Mie theory allowed application to sizing Al NPs fabricated by femtosecond laser ablation in *n*-heptane and water. In the former medium, a clear plasmon in the UV is observed, while it vanishes when the NPs are obtained in water. Optical extinction spectroscopy (OES) allowed also determining the species present in each case. Independent AFM analysis made over the same sample agrees with the sizing results derived from OES.

Acknowledgements This work was granted by PIP 0280 and PIP 0720 of CONICET; PME2006-00018 of ANPCyT; grants 11/I197 of Facultad de Ingeniería, UNLP; and X11/680 of Facultad de Cierncias Exactas, UNLP. D. C. Schinca is a member of Comisión de Investigaciones Científicas de la Provincia de Buenos Aires (CICBA), Argentina. L. B. Scaffardi, M. B. Fernández van Raap, and J. M. J. Santillán are researchers of CONICET. D. Muñetón Arboleda and L. J. Mendoza Herrera are PhD fellows of CONICET, Argentina.

References

1. Asharani PV, Sethu S, Vadukumpully S, Zhong S, Lim CT, Prakash Hande M, Valiyaveetti S (2010) Investigations on the structural damage in human erythrocytes exposed to silver, gold, and platinum nanoparticles. Adv Funct Mater 20:1233–1242
2. Takamiya M, Miyamoto Y, Yamashita T, Deguchi K, Ohta Y, Ikeda Y, Matsuura T, Abe K (2011) Neurological and pathological improvements of cerebral infarction in mice with platinum nanoparticles. J Neurosci Res 89:1125–1133
3. Zhang Y, Yuan R, Chai Y, Wang J, Zhong H (2012) Amperometric biosensor for nitrite and hydrogen peroxide based on hemoglobin immobilized on gold nanoparticles/polythionine/platinum nanoparticles modified glassy carbon electrode. J Chem Technol Biotechnol 87:570–574
4. Zhao K, Zhuang S, Chang Z, Songm H, Dai L, He P, Fang Y (2007) Amperometric glucose biosensor based on platinum nanoparticles combined aligned carbon nanotubes electrode. Electroanalysis 19: 1069–1074
5. Wang Q, Yun Y (2013) Nanoenzymatic sensor for hydrogen peroxide based on electrodeposition on silver nanoparticles on poly(ionic liquid) stabilized grapheme sheets. Microchim Acta 180:261–268
6. Elder A, Yang H, Gwiazda R, Teng X, Thurston S, He H, Oberdörster G (2007) Testing nanomaterials of unknown toxicity: an example based on platinum nanoparticles of different shapes. Adv Mater 19:3124–3129
7. Martinez-Gutierrez F, Olive PL, Banuelos A, Orrantia E, Nino N, Morales Sanchez E, Ruiz F, Bach H, Av-Gay Y (2010) Synthesis, characterization, and evaluation of antimicrobial and cytotoxic effect of silver and titanium nanoparticles. Nanomedicine: Nanotechnology, Biology and Medicine 6:681–688
8. Barr JL, Axelbaum RL, Macias ME (2006) Processing salt-encapsulated tantalum nanoparticles for high purity, ultra high surface area applications. J Nanopart Res 8:11–22
9. Katabi G, Koltypin Y, Cao X, Gedanken A (1996) Self-assembled monolayer coatings of iron nanoparticles with thiol derivatives. J Cryst Growth 166:760–762
10. De La Cruz W, Gallardo-Vega C, Tougaard S, Cota L (2008) Growth mechanism of iron nanoparticles on (0001) sapphire wafers. Microelectron J 39:1374–1375
11. Kato H, Minami T, Kanazawa T, Sasaki Y (2004) Mesopores created by platinum nanoparticles in zeolite crystals. Angew Chem 116:1271–1274
12. Park H, Choi W (2005) Photocatalytic conversion of benzene to phenol using modified TiO_2 and polyoxometalates. Catal Today 101:291–297
13. Xu C, Kang Shen P, Liu Y (2007) Ethanol electrooxidation on Pt/C and Pd/C catalysts promoted with oxide. J Power Sources 164:527–531
14. Knight MW, Liu L, Wang Y, Brown L, Mukherjee S, King NS, Everitt HO, Nordlander P, Halas NJ (2012) Aluminum plasmonic nanoantennas. Nano Lett 12:6000–6004
15. Castro-Lopez M, Brinks D, Sapienza R, van Hulst NF (2011) Aluminum for nonlinear plasmonics: resonance-driven polarized luminescence of Al, Ag, and Au nanoantennas. Nano Lett 11: 4674–4678
16. Hylton N P, Li X F, Giannini V, Lee K -H, Ekins-Daukes N J, Loo J, Vercruysse D, Van Dorpe P, Sodabanlu H, Sugiyama M and Maier S A 2013 Loss mitigation in plasmonic solar cells: aluminium nanoparticles for broadband photocurrent enhancements in GaAs photodiodes. Sci Rep. 3, N° 2874 doi:10.1038/srep02874
17. Ng S-H, Patey TJ, Büchel R, Krumeich F, Wang J-Z, Liu H-K, Pratsinis SE, Novák P (2009) Flame spray-pyrolyzed vanadium oxide nanoparticles for lithium battery cathodes. Phys Chem Chem Phys 11:3748–3755
18. Mendoza Herrera LJ, Muñetón Arboleda D, Schinca DC, Scaffardi LB (2014) Determination of plasma frequency, damping constant, and size distribution fron the complex dielectric function of noble metal nanoparticles. J Appl Phys 116:233105-1–233105-8
19. Muñetón Arboleda D, Santillán JMJ, Mendoza Herrera LJ, Fernández van Raap MB, Mendoza Zélis P, Muraca D, Schinca DC, Scaffardi LB (2015) Synthesis of Ni nanoparticles by femtosecond laser ablation in liquids: structure and sizing. J Phys Chem C 19(23):13184–13193
20. Bohren CF, Huffman DR (1998) Absorption and scattering of light by small particles. John Wiley & Sons, New York
21. Fox M (2001) Optical properties of solids. Oxford University Press, Oxford
22. Kreibig U, Vollmer M (1995) Optical properties of metal clusters. Springer-Verlag, Berlin
23. Ordal MA, Bell RJ, Alexander RW, Newquist LA, Querry MR (1988) Optical properties of Al, Fe, Ti, Ta, W, and Mo at submillimeter wavelengths. Appl Opt 27:1203–1209
24. Rakić AD, Djurišić AB, Elazar JM, Majewski ML (1998) Optical properties of metallic films for vertical-cavity optoelectronic devices. Appl Opt 37:5271–5283
25. Shiles E, Sasaki T, Inokuti M, Smith DY (1980) Self-consistency and sum-rule tests in the Kramers-Kronig analysis of optical data: applications to aluminum. Phys Rev B 22:1612–1626
26. Weaver JH, Lynch DW, Olson CG (1974) Optical properties of V, Ta, and Mo from 0.1 to 35 eV. Phys Rev B 10:501–516

27. Johnson PB, Christy RW (1974) Optical constants of transition metals: Ti, V, Cr, Mn, Fe, Co, Ni, and Pd. Phys Rev B 9:5056
28. Boyd R W 2008 Nonlinear optics (Academic Press)
29. Kittel C (1987) Quantum theory of solids. John Wiley & Sons, New York
30. Kreibig U, von Fragstein C (1969) The limitation of electron mean free path in small silver particles. Z Phys 224:307–323
31. Santillán J M J, Videla F A, Fernández van Raap M B, Schinca D C and Scaffardi L B 2012 Plasmon spectroscopy for subnanometric copper particles: dielectric function and core-shell sizing. J. Appl. Phys. 112 054319–1 to 054319–8
32. Santillán J M J, Videla F A, Fernández van Raap M B, Muraca D, Scaffardi L B and Schinca D C 2013 Influence of size-corrected bound electron contribution on nanometric silver dielectric function. Sizing through optical extinction spectroscopy. J. Phys. D: Appl. Phys. 46 435301–1 to 435301–10
33. Scaffardi LB, Tocho JO (2006) Size dependence of refractive index of gold nanoparticles. Nanotechnology 17:1309–1315
34. Kachhava CM (2003) Solid state physics, solid state device and electronics. New Age International Publishers, New Delhi
35. Panda BP (2012) Electronic structure and equilibrium properties of hcp titanium and zirconium. J Phys 79:327–335
36. Mattheiss LF (1970) Electronic structure of niobium and tantalum. Phys Rev B 1:373–381
37. Ketterson JB, Windmiller LH, Hörnfeldt S, Mueller F (1968) Fermi velocity and Fermi radius in platinum. Solid State Commun 6:851–854
38. Fouad SS, El-Fazary MH, El-Shazly AA, Sharaf F, Nassr KM (1991) Optical properties of vanadium thin films. J Mater Sci 26: 5843–5847
39. Santillán J M J, Videla F A, Fernández van Raap M B, Schinca D C and Scaffardi L B 2013 Analysis of the structure, configuration, and sizing of Cu and Cu oxide nanoparticles generated by fs laser ablation of solid target in liquids. J. Appl. Phys. **113** 134305–1 to 134305–9
40. Zheng BY, Wang Y, Nordlander P, Halas NJ (2014) Color-selective and CMOS-compatible photodetection based on aluminum plasmonics. Adv Mater 26:6318–6323
41. Jiao X, Wang Y, Blair S (2015) Efficient UV photocatalysis assisted by densely distributed aluminum nanoparticles. J Phys D Appl Phys 48:1–6
42. Honda M, Kumamoto Y, Taguchi A, Saito Y, Kawata S (2015) Efficient UV photocatalysis assisted by densely distributed aluminum nanoparticles. J Phys D Appl Phys 48:1–6
43. Mao J, Blair S (2015) Nanofocusing of UV light in aluminum V-grooves. J Phys D Appl Phys 48:1–10